Electronic Supplementary Material (ESI) for Biomaterials Science.

Supplemental information for

Transient binding promotes molecule penetration into mucin hydrogels by enhancing molecular partitioning

Matthias Marczynski*[,1], Benjamin T. Käsdorf*[,1], Bernhard Altaner[2], Andreas Wenzler[1], Ulrich Gerland[2], and Oliver Lieleg#[,1]

[1] Department of Mechanical Engineering and Munich School of Bioengineering,

Technical University of Munich, Boltzmannstrasse 11, 85748, Garching, Germany

[2] Physics Department, Technical University of Munich, James-Frank-Strasse 1, 85748 Garching, Germany

#: correspondence: oliver.lieleg@tum.de

*: equal contribution

1. Biochemical characterization of the manually purified gastric mucin

To clarify whether our purified gastric mucin preparation contains both variants of naturally occurring gastric mucins (i.e., MUC5AC and MUC6), we employed a double-stain using lectins. Manually purified gastric mucin was rehydrated in ultrapure water (final concentration: 1 % (w/v)) and incubated with 10 µg mL^{-1} wheat germ agglutinin (WGA). This lectin is labelled with the red fluorophor tetramethylrhodamine (TRITC) that binds to sialic acid residues present in MUC5AC and MUC6; thus, this lectin label confers red fluorescence to both gastric mucin variants. Then, 5 µg mL^{-1} of the fluorescein isothiocyanate (FITC, green signal) conjugate of lectin from *Griffonia simplicifolia* (GSA-II, this lectin specifically binds to terminal α-1,4-linked *N*-acetylglucosamine residues which are only present in MUC6), were added to test for the presence of MUC6 molecules by green fluorescence signals. The mucin solution was acidified to pH 2 to induce gel formation, and images of the mucin gel were recorded on a fluorescence microscope.

Indeed, the overlay image in Fig. S1 shows a co-localization of both fluorescence signals, which proves the presence of MUC6 molecules in our manually purified gastric mucin.

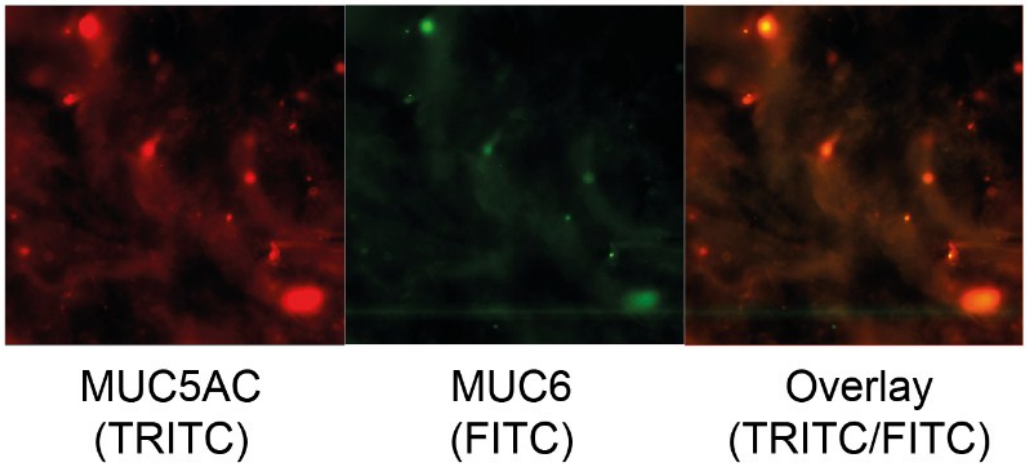

Figure S1: Co-localization experiments demonstrate the presence of MUC6 in manually purified gastric mucin. Red-fluorescing TRITC-WGA binds to sialic acid residues, thus labeling mucin molecules in general. The green fluorescing FITC-GSA II specifically binds to terminal α-1,4-linked *N*-acetylglucosamine residues, which are present in MUC6 but not in MUC5AC. The co-localization of both fluorescence signals in mucin gels proves the presence of MUC6 molecules in manually purified gastric mucin.

2. Tapered design of the microchannel tips

For our microfluidics experiments, we designed the geometry of the mucin-gel microchannels such, that they offer a slight resistance when a solution of purified mucins is injected: the channels narrow at their 'tips' as shown in the schematic below. In addition to providing an increase mechanical resistance, this particular channel geometry also influences the shape of the liquid interface at the finger tips since the surface of the two opposing PDMS channels are now slightly tilted towards each other and the resulting wetting process is affected by this as explained in the schematic images. Indeed, in our chips, we observe a relatively flat interface at the PDMS/liquid/air interface which makes the following penetration experiments easier to quantify.

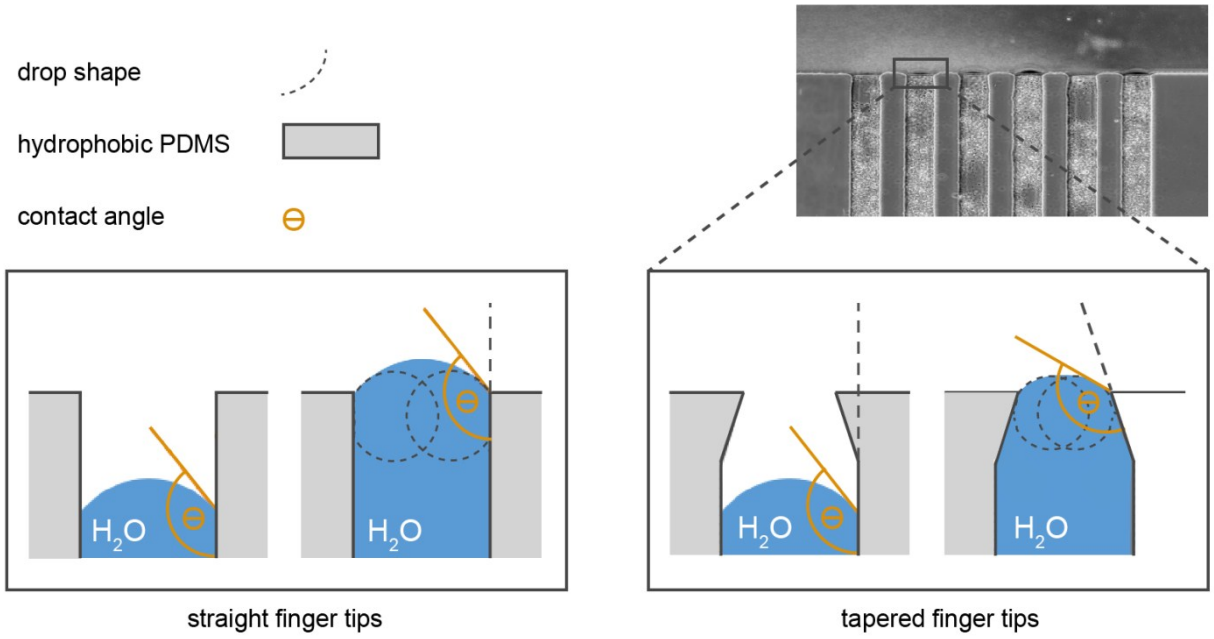

Figure S2: The dedicated design of the microfluidic channels facilitates their filling and creates a flat gel/buffer interface which enables a proper evaluation of the ensuing penetration experiments. *Left schematic:* When microchannels with straight ends are filled with an aqueous mucin solution, a convex interface is formed which reaches into the buffer compartment and, thus, is relatively unstable when the liquid in the buffer compartment is exchange. *Right schematic*: A stable, flat interface is achieved, when a chip design with tapered 'fingers' is used. The improved channel geometry does not affect the contact angle between water and PDMS but induces a tilt of the two opposing PDMS surfaces during the wetting process. This effect is responsible for the flatter interface created during microchannel filling.

3. Gel formation of gastric and intestinal mucin solutions at acidic pH

As established for gastric mucins in the literature, lowering the buffer pH from neutral to acidic conditions should change the properties of mucin solutions from a viscoelastic fluid (dominated by the loss modulus *G''*) to a viscoelastic gel (dominated by the storage modulus *G'*) [1-4]. To test for the gel-forming abilities of our purified mucins and to determine the viscoelastic properties of the hydrogels created by them, rheological measurements were conducted with 1 % (w/v) solutions of purified porcine mucins (either MUC5AC or MUC2)

Lyophilized mucin was weighed and rehydrated in 9 parts of ultrapure water during shaking at 4 °C at 400 rpm in a thermomixer (Thermomixer comfort, Eppendorf, Hamburg, Germany). Prior to analysis, his hydrated mucin solution was then mixed with 1 part of either 100 mM phosphate buffer (pH 7.0) or 100 mM acetate buffer (pH 4.0), respectively. The rheological evaluation of mucin solutions and gels was performed on a stress-controlled shear rheometer (MCR 302, Anton Paar, Graz, Austria) using a plate/plate measuring setup (PP25, Anton Paar) and 150 µm plate separation. Oscillating shear measurements for determining the frequency dependent viscoelastic moduli were conducted in a strain controlled mode. 100 µL of sample were used for each measurement, and the storage modulus *G'* and loss modulus *G''* were recorded within a frequency range of 0.1 – 7 Hz. The temperature during each measurement was set to 20 °C.

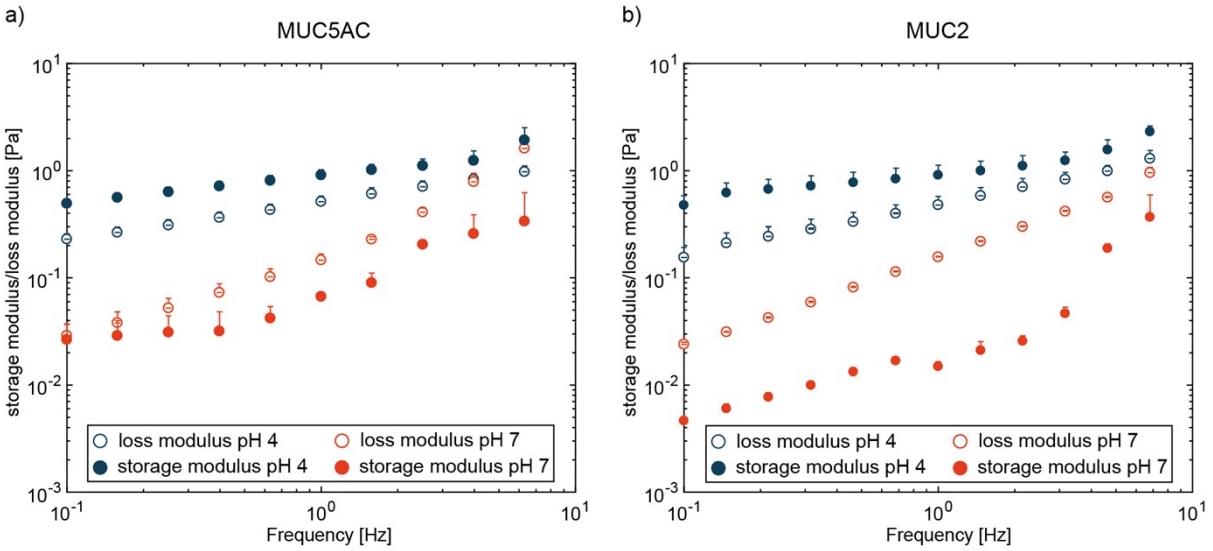

Figure S3: Gelation of gastric and intestinal mucin solutions. The viscoelastic frequency response of mucin samples is shown for both neutral and acidic buffer conditions. Closed symbols denote the storage modulus *G'* and open symbols the loss modulus *G''*. At neutral pH (red symbols), 1 % (w/v) solutions of both MUC5AC (a) and MUC2 (b) are dominated by viscous properties over the whole measured frequency range. In contrast, at an acidic pH of 4.0, solutions of MUC5AC and MUC2 (blue symbols) both formed hydrogels, which are dominated by elastic properties. Error bars represent the standard error of the mean as obtained from three independent measurements.

---

1. Celli, J.P., et al., *Rheology of gastric mucin exhibits a pH-dependent sol-gel transition.* Biomacromolecules, 2007. **8**(5): p. 1580-6.
2. Cao, X.X., et al., *pH-dependent conformational change of gastric mucin leads to sol-gel transition.* Biophysical Journal, 1999. **76**(3): p. 1250-1258.
3. Bhaskar, K.R., et al., *Profound Increase in Viscosity and Aggregation of Pig Gastric Mucin at Low Ph.* American Journal of Physiology, 1991. **261**(5): p. G827-G833.
4. Lai, S.K., et al., *Micro- and macrorheology of mucus.* Adv Drug Deliv Rev, 2009. **61**(2): p. 86-100.

4. Non-normalized penetration profiles of DEAE-dextrans into MUC5AC gels

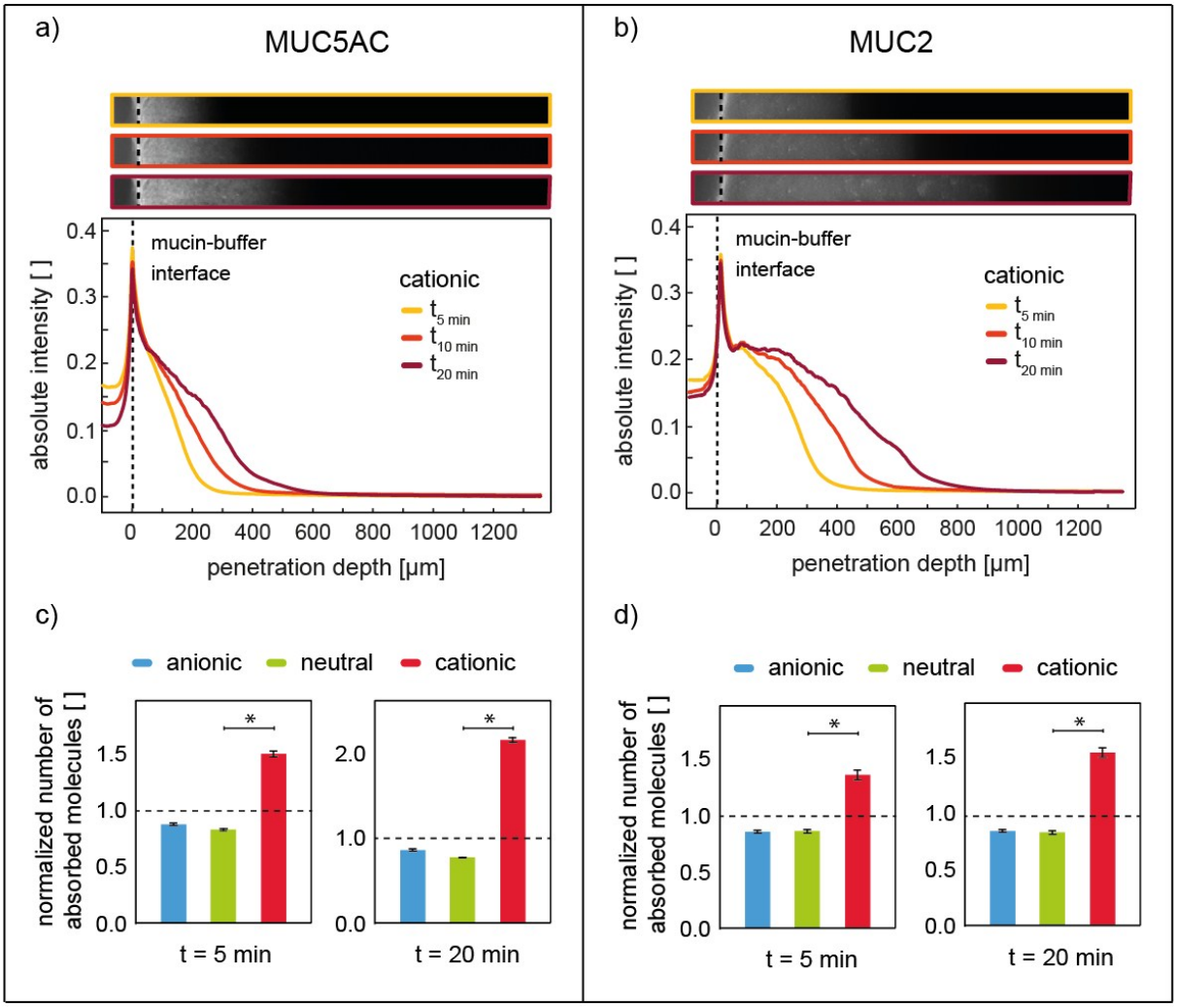

Figure S4: Non-normalized penetration profiles of cationic dextrans into mucin gels. (a, b) The barrier properties of mucin gels reconstituted from porcine gastric mucin MUC5AC (a) towards cationic DEAE-dextrans are compared to gels comprising purified porcine intestinal mucin MUC2 (b). Different from the curves shown in Fig. 3 of the main paper, the fluorescence intensity profiles determined at different time points of the experiment were not normalized and thus can contain photobleaching effects or other artefacts. However, those non-normalized profiles demonstrate that the height of the dextran accumulation peak does not increase over time and that the concentration of dextran molecules in the buffer compartment decreases as the penetration experiment progresses. Both effects are consistent with the calculated penetration profiles shown in Fig. 4a and Fig. S7a.
(c, d) The same qualitative difference in the partitioning behavior of the three dextran variants depicted in Fig. 3c,d of the main paper for a penetration time of 10 min is also observed for shorter (5 min) and larger (20 min) penetration times. The number of molecules absorbed into the first 50 µm of the mucin gel is normalized to the number of molecules that would be present in this gel region if the local dextran concentration in the gel would be identical to that in the buffer reservoir (indicated as dashed line). The error bars denote the standard error of the mean as obtained from analyzing at least seven 'fingers' each.

5. Local fluorescence depletion zone near the buffer/gel interface

In addition to an accumulation of positively charged DEAE-dextrans at the buffer/gel interface, a depletion of molecules (i.e., a darker area) is observed right in front of the buffer/gel interface:

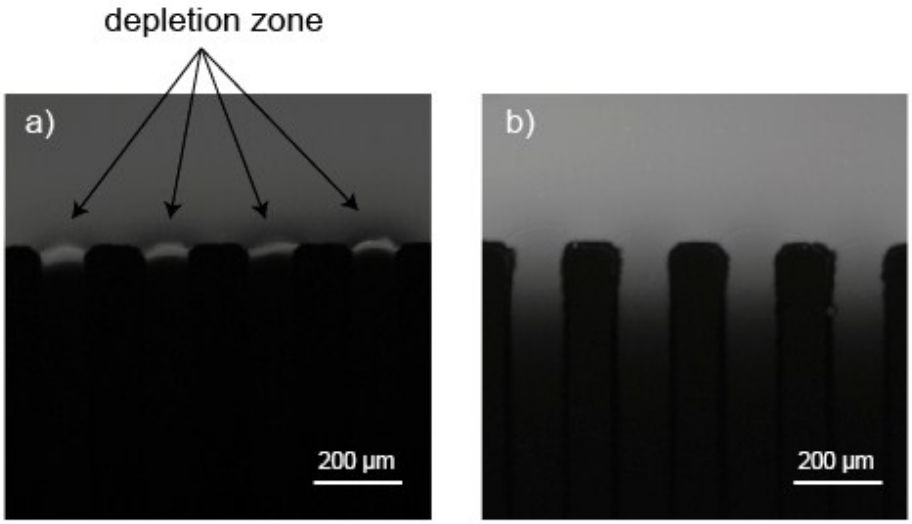

Figure S5: Close-up images of the buffer/gel interface taken immediately after filling of the test reservoir of a microfluidic chip with a solution of either positively charged (a) or negatively charged dextran molecules (b). In addition to an accumulation at the gel/buffer interface, a local depletion of cationic DEAE-dextran molecules in front of the interface (darker areas) was observed (a). In contrast, for anionic CM-dextrans, neither an accumulation nor a local depletion occurred (b). Images were acquired with a 4x objective (HI PLAN 4x/0.10 NA, Leica). The scale bars represent 200 µm.

6. Evaluating the binding interaction between dextran molecules and mucins

For testing the binding affinity of the three different dextran variants towards mucin layers, we immobilized mucin MUC5AC from ten different purification batches (or MUC2 from three different purification batches) via physisorption onto the bottom of the wells of 96-well plates. For this purpose, lyophilized mucin was first rehydrated at a concentration of 0.5 % (w/v), and 150 µL of a mucin solution were filled into each well. For each mucin batch, 15 wells were prepared. After incubation at 4 °C overnight, the mucin solutions were discarded, and the wells were rinsed twice with 10 mM acetate buffer (pH 4.0). Afterwards, each well was filled with 60 µL of a dextran solution (0.02 % (w/v) in 10 mM acetate buffer, pH 4.0). Five wells per mucin batch and dextran variant (cationic, neutral and anionic) were filled with a dextran solution. Additionally, for each dextran variant, five uncoated wells were filled with a dextran solution as a reference. After incubation at room temperature for 4 h, 50 µL were transferred from each well to new 96-well plates, and the fluorescence intensity was determined for each well at a wavelength of $\lambda_{535\ nm}$ using a VICTOR3 V Multilabel Counter (PerkinElmer, Waltham, MA, USA).

The fraction of dextran molecules that remained in the solution (Fig. S2) was then calculated as the ratio of the fluorescence intensity of dextran solutions that were incubated in a mucin-coated well and the fluorescence intensity of dextran solutions that were incubated in an uncoated reference well. The relative affinity *a* (see main paper Fig. 3c, d) of the three dextran variants was then determined according to

$$a = \frac{(1 - F_{retained})}{F_{retained,\ neutral}} = \frac{F_{adsorbed}}{F_{retained,\ neutral}}$$

where $F_{retained}$ denotes the fraction of dextran molecules that were retained in solution and $F_{retained,\ neutral}$ the fraction of neutral dextrans that were retained in solution. These are also the values which are (after normalization to the value obtained for unmodified dextran) given in Fig. 3c and d of the main manuscript.

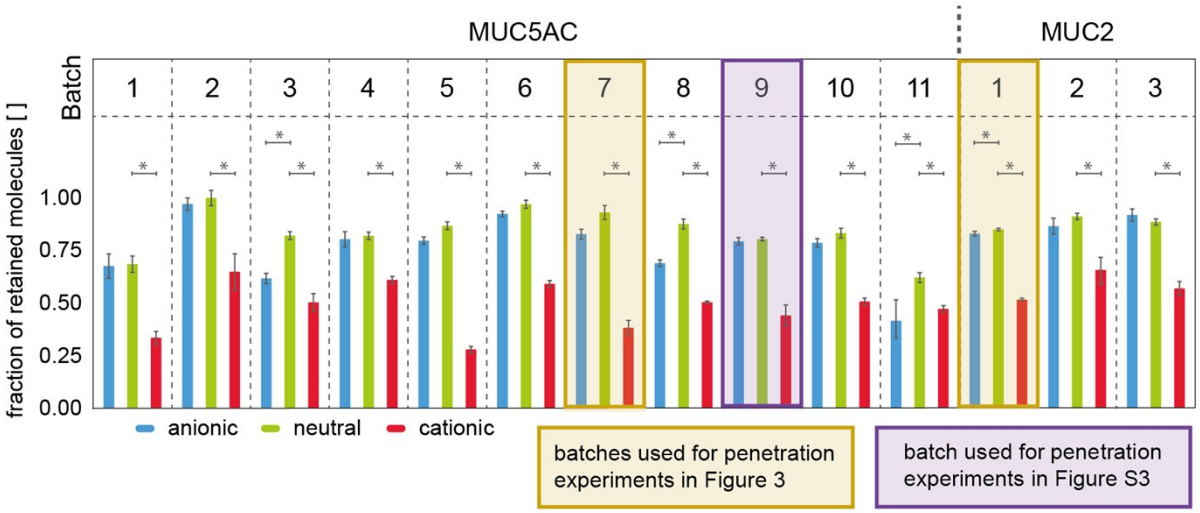

Figure S6: Adsorption efficiency of different dextran variants to surface coatings performed with purified gastric mucin MUC5AC and purified small intestinal mucin MUC2, respectively. The adsorption behavior of three different dextran variants to layers of gastric mucin or small intestinal mucin, respectively, is compared by a depletion assay (see text above). In all tested mucin batches, cationic dextrans show the highest adsorption efficiency. However, the amount of depleted cationic dextrans varies within the different batches. For at least two batches of gastric mucin (batch 3 and 8), an increased adsorption of anionic dextrans – compared to neutral dextrans – is observed. The error bars denote the standard error of the mean.

For statistical analysis of the results obtained from depletion experiments, the software R together with the user interface RStudio (version 3.4.2, September 2017) was used. At least three independent measurements were evaluated for each tested combination of dextran variant and mucin batch. The obtained data distributions were first checked for normality by Q-Q plots and a Shapiro-Wilk test, and homogeneity of variances was confirmed by a Levene test. To detect significant differences in the fraction of retained molecules obtained with this depletion assay for three different dextran variants, two-sample independent (two-tailed) *t*-tests were conducted. Data obtained for unmodified dextrans was always used as a reference point. Since variances were homogeneous, Student's *t*-tests were performed. The level for significant differences was set to a *p*-value of $p < 0.05$.

7. Penetration behavior of dextrans into mucin gels reconstituted from a different batch of MUC5AC

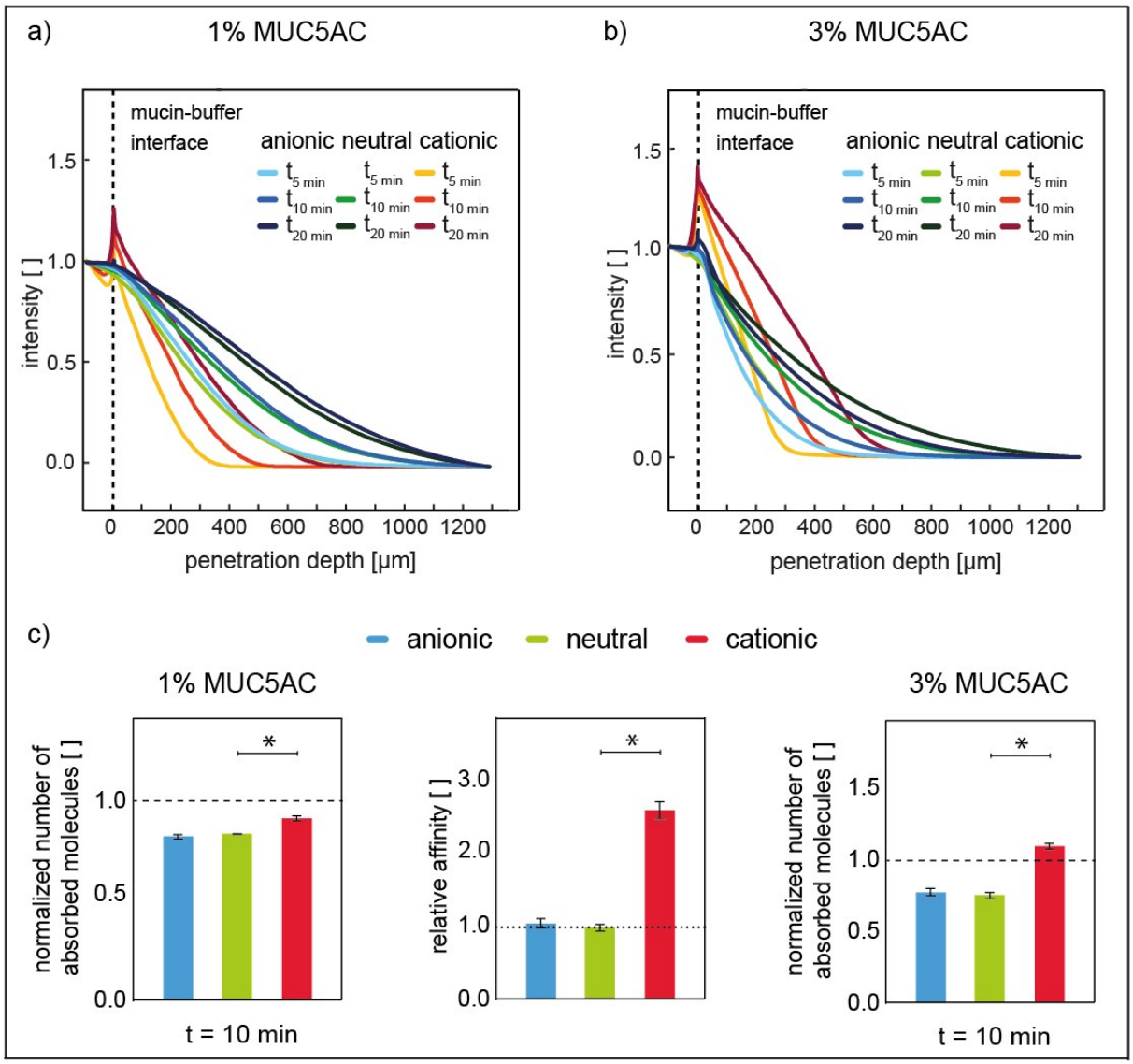

Figure S7: Penetration behavior of different dextran variants into porcine gastric mucin gels reconstituted at mucin concentrations of 1% (a) and 3% (b), respectively. (a, b) The data shown in this graph was obtained with MUC5AC purification batch 9 (see Fig. S5) whereas MUC5AC purification batch 7 and MUC2 purification batch 1 were used for penetration experiments depicted in the main paper. Also here, the diffusive penetration behavior of cationic dextrans differs from that of both neutral and anionic dextrans. The former accumulate at the buffer/mucin interface whereas the latter two show penetration profiles with local concentrations that continuously decrease with increasing channel depth. (c) *Left and right*: For penetration times of ten minutes, the number of absorbed DEAE-dextrans significantly exceeds that of non-binding neutral dextrans. However, the local DEAE-dextran concentration within the first 50 µm of the 1 % (w/v) mucin gel is lower than the number of molecules that would be present in the mucin gel if the local dextran concentration in the gel would be identical to that in the buffer reservoir (indicated as a dashed line). At an increased mucin concentration of 3 % (w/v) the partitioning of cationic molecules into the mucin gel is enhanced, whereas the partitioning of neutral and anionic dextrans appears unaffected. Now, the cationic DEAE-dextrans reach higher local concentrations in the first 50 µm of the mucin gel than in the buffer reservoir. The error bars denote the standard error of the mean as obtained from analyzing at least seven 'fingers' each in (a) and (c, left) and 13 'fingers' each in (b) and (c, right). (c) *Middle*: For the mucin batch used here, cationic dextrans show a ~2.5fold affinity towards mucin coated surfaces compared to neutral and anionic dextrans for gastric mucins. The binding affinity of neutral dextrans to mucin surfaces is set to one and indicated by a dotted line; the error bars denote the standard error of the mean as obtained from five wells analyzed in a dextran depletion assay.

8. Locally increased mucin concentration at the gel/buffer interface

To detect differences in the local concentration of mucins within reconstituted mucin gels on-chip, solutions of 1 % (w/v) MUC5AC and MUC2, respectively, were pre-mixed with 10 µg/mL of fluorescently labeled wheat germ agglutinin, which specifically binds to sialic acid residues. The solutions of lectin-labeled mucins were filled into microfluidics chips and a stable gel/buffer interface was generated as described in the main text. Fluorescence images were then acquired on a DMi8 Leica microscope (Leica, Wetzlar, Germany) using a 4x objective (HI PLAN 4x/0.10, Leica) with a digital camera (Orca Flash 4.0 C114400, Hamamatsu, Japan).

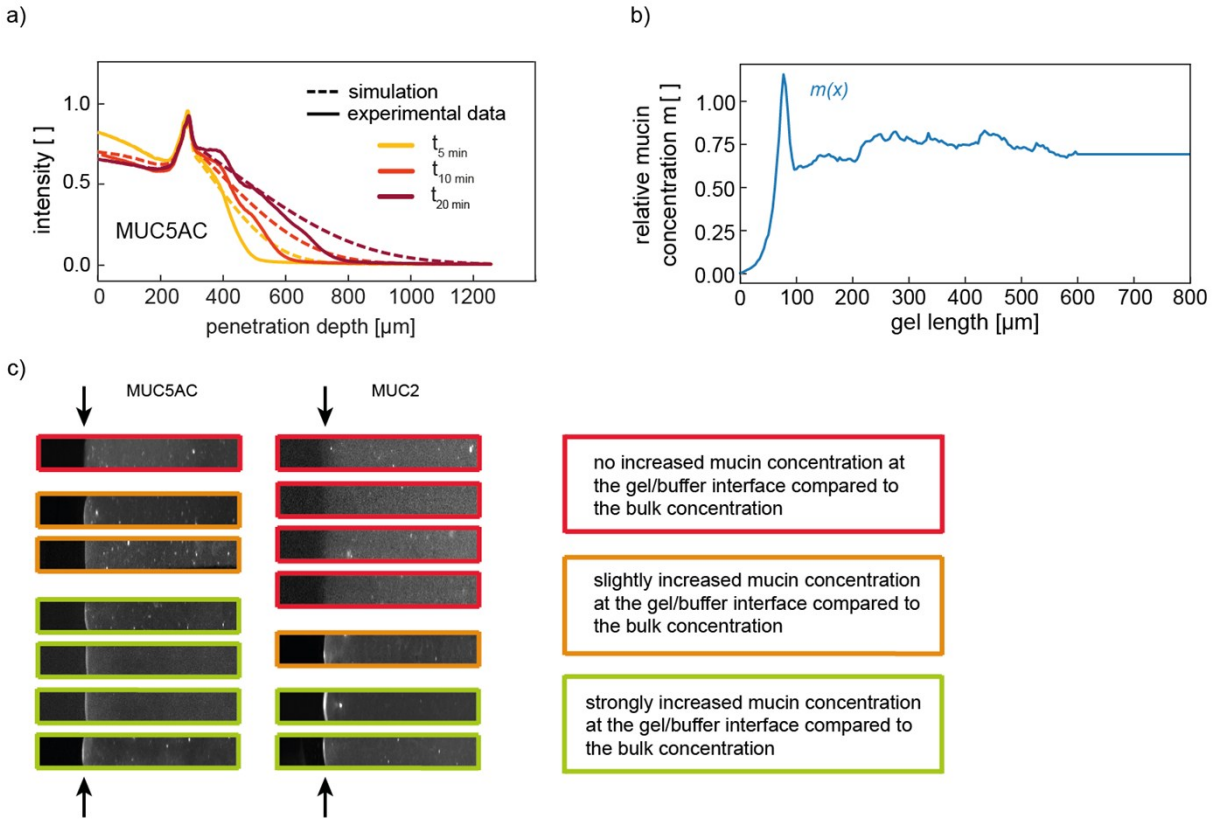

Figure S8: Reconstituted mucin gels exhibit an increased mucin concentration at the gel/buffer interface. (a) The simulated penetration profiles agree reasonably well with the experimentally obtained penetration profiles of cationic dextrans into reconstituted MUC5AC hydrogels (the experimental profile represents an average obtained from four 'fingers'). (b) By combining results from the simulation with experimental data (shown in Fig. 4a) in a self-consistent iterative scheme, an averaged profile for the local mucin concentration within the four 'fingers' is obtained. This extracted mucin concentration profile $m(x)$ is almost constant in the bulk phase of the gel but exhibits a clear peak at the gel/buffer interface. (c) Exemplary fluorescence images of seven gel 'fingers' filled with a fluorescently labelled MUC5AC and MUC2 gel, respectively. For the majority of the MUC5AC gels, a locally increased mucin concentration at the gel/buffer interface is observed compared to the mucin concentration in the bulk phase of the gel. For MUC2 gels, such a locally increase mucin concentration at the buffer/gel interface can also be detected, albeit less frequently as for MUC5AC gels. The arrows indicate the position of the gel/buffer interface to guide the eye.

The fluorescence intensity correlates with the mucin concentration: A bright signal at a certain gel location indicates a high local mucin concentration, whereas a weak fluorescence signal corresponds to a low local mucin concentration. Locally increased mucin concentrations can be detected at the gel/buffer interface for the majority of the MUC5AC

gels, whereas this is only the case for some MUC2 gels. Also, the amount of such locally increased mucin concentration can vary. At this point, we can only speculate as to why this effect occurs at the buffer/gel interphase. One possible explanation might be that this is an interfacial phenomenon arising from surface tension effects (since the mucin solution is inserted into the channels first before the acidic buffer is added to induce gelation). Alternatively, it might be a mechanical effect that is created by compressive forces that originate from filling the reservoir with buffer.

9. Reaction-diffusion model

In this section, we provide a complete reaction-diffusion equations used for the theoretical modeling discussed in the main text. The model assumes that unbound molecules with a concentration profile *u(x,t)* diffuse with diffusion coefficient *D*, while bound molecules with a concentration profile *b(x,t)* do not participate in diffusion. Binding and unbinding of molecules is modelled by a mass-action reaction current *r(x,t)*

$$r(x,t) = k^+ * u(x,t) * m(x,t) - k^- * b(x,t) ,$$

where *m(x,t)* denotes the line concentration of unoccupied binding sites and k^+ and k^- are the rate constants for binding and unbinding, respectively. Assuming a fixed total concentration of binding sites *m(x)*, we obtain

$$r(x,t) = k^+ * u(x,t) * [m(x) - b(x,t)] - k^- * b(x,t) .$$

The reaction-diffusion equations then read:

$$\frac{d}{dt}u(x,t) = D\frac{d^2}{dx^2}u(x,t) - r(x,t),$$

$$\frac{d}{dt}b(x,t) = r(x,t).$$

To solve the system, boundary and initial conditions need to be specified. We estimate the time-dependent boundary concentration for molecules in the buffer reservoir as described in the next section. This results in a boundary condition of the form $u(-s,t) = f(t)$ at the left side ($x = -s$). On the right hand side (at $x = L$) we assume absorbing boundary conditions, i.e. $u(L,t) = 0$.

For the physiological model with a retrograde flow due to mucus renewal, we assume a constant drift velocity *v* in negative x-direction. The combined reaction-diffusion-drift equations then become

$$\frac{d}{dt}u(x,t) = D\frac{d^2}{dx^2}u(x,t) - v\frac{d}{dx}u(x,t) - r(x,t),$$

$$\frac{d}{dt}b(x,t) = - v\frac{d}{dx}b(x,t) + r(x,t).$$

In all simulations with mucus renewal we chose v = 0.1 µm s^{-1}. We assumed a constant left boundary condition $u(x = 0,t) = f(t) = 1$ for the steady-state calculations. For the simulations of drug pulses we used $f(t)$ = 1 for $t < \tau_0$ and $f(t)$ = 0 for $t \geq \tau_0$.

10. Normalizing the experimental intensity profiles for quantitative analysis

For our quantitative comparisons between experimental and simulation data, we used the following image analysis procedure:

The starting point is the raw image data intensity (pictures of 45 px width and around 1800 px of height) for each finger at different times. For fingers in the same hand, that is, fingers from a single microfluidic chip, the image data for all times was cut to the same height. To reduce the two-dimensional data to a single dimension, the intensity values of the 45 lines was averaged. A second averaging was performed over the data obtained from all fingers. After that, a background normalization was performed by subtracting the minimum intensity value for each intensity curve. In all experiments, the features of the time-dependent concentration profiles (saturated plateau and peak value, as well as the diffusive shape of the profiles in the tails, see Fig. S9a) suggest that photo bleaching effects are negligible. The result of this image-analysis procedure is an average one-dimensional intensity profile for each time in one microfluidic device. We do not average over multiple microfluidic devices, because boundary conditions (and absolute intensity values) display a significant variation between experiments.

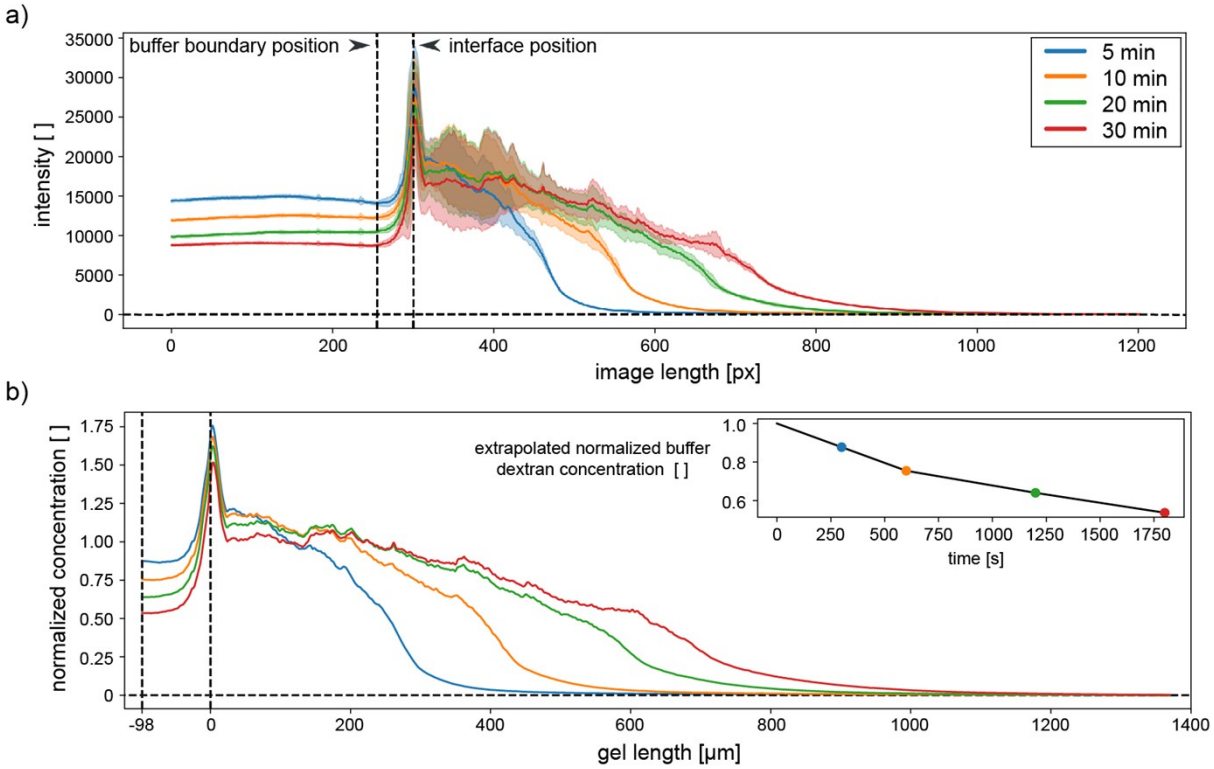

Figure S9: (a) Image intensity profiles (averaged over the "fingers" of one microfluidic device) with standard error. The two black dashed lines denote the positions of the left boundary condition (to extrapolate and gauge concentration) and the position of the interface, respectively. (b) Re-normalized concentration data with interface at x = 0 as a function of physical coordinates. The inset shows the extrapolated buffer concentration at the boundary, normalized to unity at t = 0.

Next, we convert pixel coordinates into physical space. From image analysis, the width of a single pixel was determined as 1.625 microns. The physical position $x = 0$ was then determined by identifying the interface pixel position using an estimate (elsewise, if a peak was present, using the position of the intensity maximum as $x = 0$; see Fig. S9).

We also rescale the y-axis (intensity) of the profiles by normalizing with the intensity at $t = 0$ at $t = 0$ position $x = -97.5$ µm, which we take as a proxy for the initial buffer intensity. When there is no data, we linearly extrapolate the intensity time series at the buffer boundary position to $t = 0$. The obtained values then correspond to concentrations normalized with respect to the initial concentration of dextran molecules at the start of the experiment. These profiles, together with the interpolated time-series of the buffer boundary concentrations (see inset of Fig. S9), are the input for the parameter extraction procedure described in the next section.

11. Self-consistent estimation of the mucin binding site profile

We extract *m(x)* from the averaged and normalized experimental profiles (see previous section) using a parameter estimation scheme that also provides consistent values for the rate constants k^+ and k^-. Towards this end, we assume that the *m(x)*-profile is non-uniform only in the vicinity of the interface, but takes on a constant bulk value after a cutoff distance (indicated by the dashed vertical line in Fig. S10, right column). Our parameter estimation scheme is iterative and starts by choosing trial values for the rate constants k^+ and k^-, as well as an initial guess for the *m(x)*-profile. Using these, we calculate the time-dependent concentration profiles *u(x,t)* and *b(x,t)* by solving the reaction-diffusion equations of the model numerically, with the initial and boundary conditions as extracted from the experiments (see previous section). We then use the experimental data for the total concentration and the simulated data for the unbound concentration (at the largest experimentally available time) to get an updated estimate for *m(x).* We iterate this procedure until convergence is reached (usually within three iterations) to determine a shape of the *m(x)*-profile that is self-consistent (see Fig. S10, right column).

The obtained self-consistent *m(x)*-profile that results from this procedure and, in particular, the absolute scale of *m(x)* depends on the chosen values for the rate constants. To get profiles that match the data, we vary the rate constants k^+ and k^- and repeat the self-consistent *m(x)*-estimation until agreement with the experimental data is achieved for all times (see Fig. S10, left column). Importantly, multiple combinations of rate constant values yield simulation results that adequately describe the experimental profiles. As illustrated in Fig. S10, the equilibrium constant is much better constrained by the data than the individual rate constants. Generally, the extraction of the rate constants and the *m(x)*-profiles primarily serves as a demonstration that a simple second-order mass-action binding model can indeed describe the observed behavior.

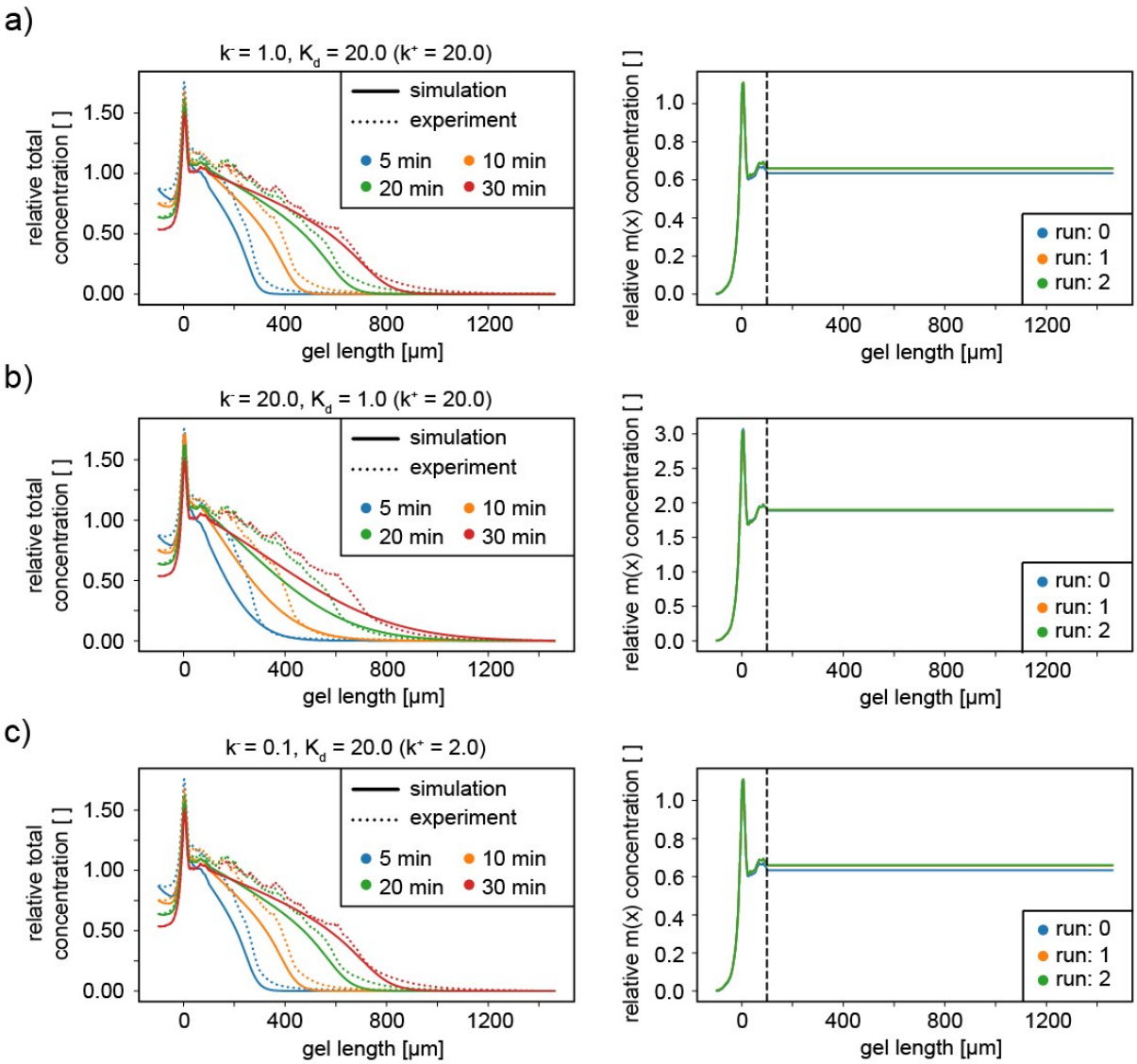

Figure S10: Comparison of experiments (as obtained for a set of 'fingers' of one 'hand' filled with intestinal mucin MUC2 gels and positively charged dextrans) with simulations (left panel), and extracted $m^{(x)}$ concentration profile (right panel) for different parameter values. In the $m^{(x)}$ profile a cut-off position is used, after which it is assumed to be constant to ensure convergence. The ratio of the transition rates $K_d = k^+/k^-$ is the most important parameter. (a) The values $k^+ = 20$, $k^- = 1$ give the best fit for this dataset, and are thus used in the simulations. (b) Parameter values that give a worse fit ($k^+ = 20$, $k^- = 20$). A low K_d also leads to a different scale of the estimated $m^{(x)}$ concentration. (c) A similarly good fit as in (a) is achieved with lower rates but same K_d.

12. Simulated penetration profiles into self-renewing mucin gels - stationary case

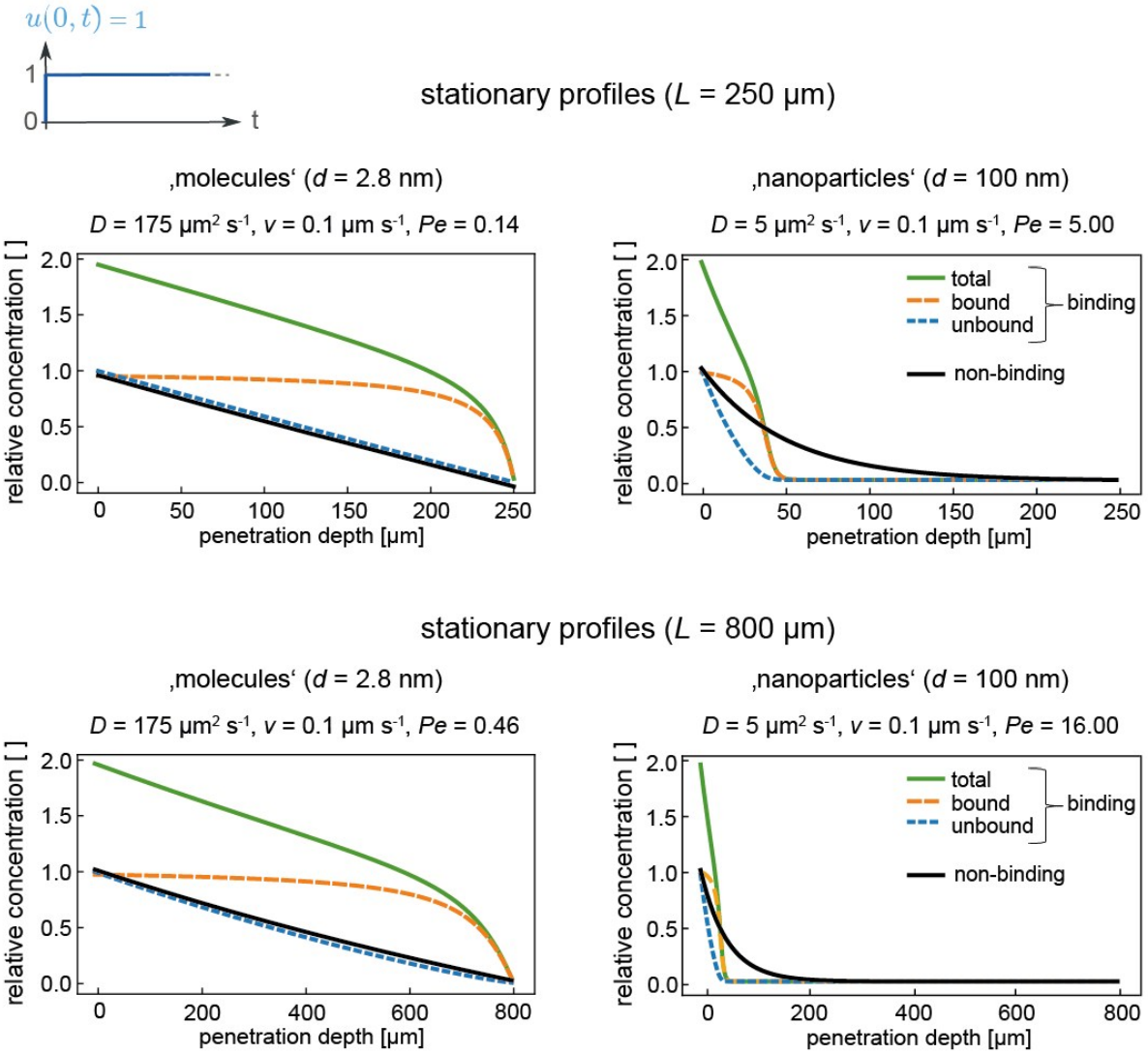

Figure S11: Stationary penetration profiles as obtained for simulated molecules or nanoparticles when a constant molecule/nanoparticle concentration at the mucus surface is assumed. The rate constants k^+, k^- are the same as in those used in the main paper, and a constant mucin concentration profile $m(x) = m_0 = 1$ is applied. Mucus self-renewal is modelled by assuming a constant retrograde flow with a velocity of v = 0.1 µm s^{-1}. *Left:* For small molecules (D = 175 µm^2 s^{-1}) transient binding to the hydrogel macromolecules barely affects the concentration profile of unbound molecules, even at a large mucus thickness of L = 800 µm. *Right:* For larger diffusing objects such as nanoparticles (D = 5 µm^2 s^{-1}), the concentration profile of freely diffusing (and thus transported) objects with the same binding parameters (blue, dashed curve) is significantly reduced compared to inert, non-binding objects (black, solid curve). At the largest modelled mucus gel thickness of L = 800 µm, even non-binding nanoparticles cannot penetrate the thick, self-renewing mucus gel.

13. Simulated translocation efficiency of molecules across self-renewing mucin gels – 'drug pulse' scenario

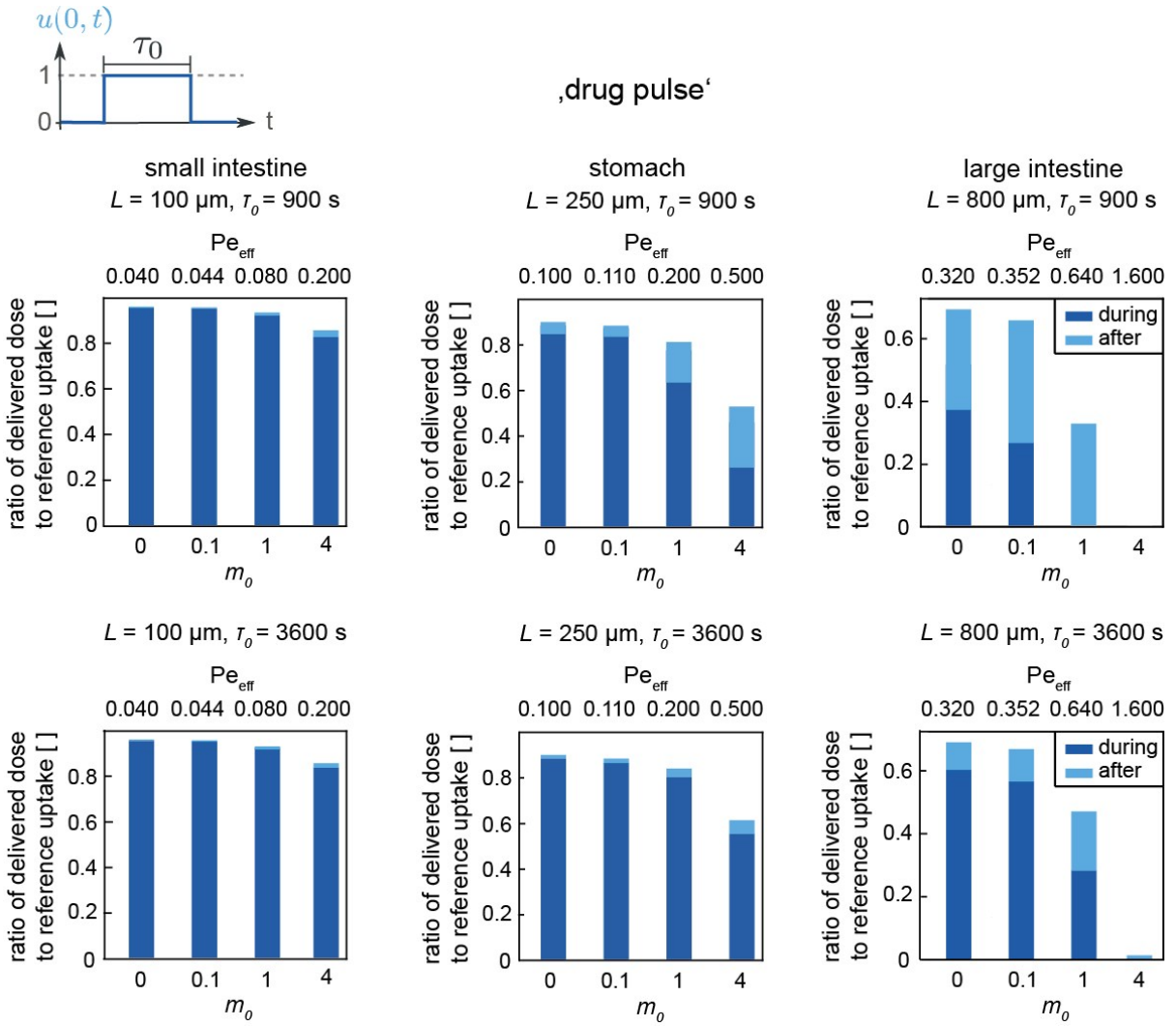

Figure S12: Simulated absorption behavior of small 'molecules' (D = 175 µm² s⁻¹) at the right boundary of a self-renewing mucus gel. Mucus self-renewal is modelled by assuming a constant retrograde flow with a velocity of v = 0.1 µm s^{-1}. Scenarios with different mucus gel thicknesses L_i are compared for different, spatially constant (bulk) mucin concentrations m_0 in a 'drug pulse' scenario. Data is shown for two different drug pulse durations, τ_0 = 900 s and τ_0 = 3600 s. Dark blue bars ('during') indicate the ratio of the delivered dose of molecules normalized to the reference molecules uptake during the duration of the pulse, light blue bars ('after') indicate the ratio of the absorbed dose of molecules normalized to the reference molecules uptake after the pulse has ended. For stronger binding, a larger fraction of molecules bind to the gel and unbind only after the pulse has passed; this induces an effect of delayed drug delivery ('after') which becomes increasingly important for thicker mucus barriers.

14. Gelation of MUC5AC solutions and penetration of cationic dextrans into MUC5AC gels at pH 1

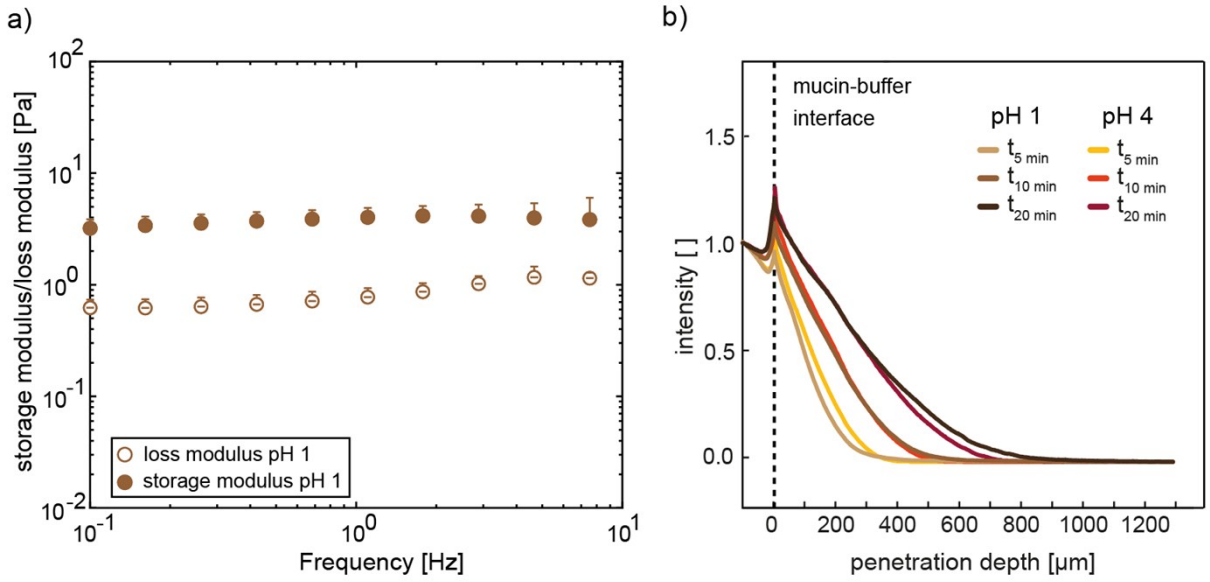

Figure S13: Gelation of gastric mucin solutions at pH 1 and penetration of positively charged dextran molecules into such mucin gels. (a) The viscoelastic frequency response of a gastric mucin sample reconstituted in acidic buffer at pH 1 is shown. Closed symbols denote the storage modulus *G'* and open symbols the loss modulus *G''*. The mucin sample is dominated by elastic properties over the whole measured frequency range (0.1 – 7 Hz). Error bars denote the standard error of the mean as obtained from three independent measurements. (b) All data shown in this graph was obtained using mucin solutions from the same batch (batch 9; see Fig. S5) at a concentration of 1 % (w/v). At both pH levels, the dextran molecules accumulated at the gel/buffer interface and showed virtually identical penetration profiles into the MUC5AC gel. Profiles shown were obtained from eleven 'fingers' (pH 1) and 33 'fingers' (pH 4), respectively.

15. Estimation of the diffusion coefficient of dextran molecules in mucin gels

The diffusive travel distance (mean squared displacement, $< x^2 >$) of a molecule in a viscous medium after a given time span *t* is linked to the molecules' diffusion coefficient *D* and the spatial dimension *n* via

$$< x^2 > = 2 * n * D * t .$$

The diffusion coefficient *D* satisfies the Einstein-Smoluchowski relation

$$D = \frac{k_B * T}{6 * \pi * \eta * R},$$

with $k_B T$ denoting the thermal energy, η the viscosity of the medium and R the hydrodynamic radius of the diffusing molecule. For a molecule diffusing in a gel, one obtains an effective diffusion coefficient for diffusion over length scales larger than the mesh size of the gel. While this effective diffusion coefficient is smaller than the free diffusion coefficient, this effect is insignificant in the parameter regime explored by our experiments, since the hydrodynamic radius of our molecules is considerably smaller than the mesh size of the gel (see also the discussion in the main text). When we assume a local water-like viscosity within the mucin gel and a hydrodynamic radius $R = 1.4\ \text{nm}$ for the 4 kDa dextran molecules (given by the supplier, Sigma Aldrich), we obtain the following diffusion coefficient at room temperature ($T = 25\ ^\circ\text{C}$):

$$D = \frac{1.38 * 10^{-23} \frac{\text{kg} * \text{m}^2}{\text{s}^2 * \text{K}} * 298\ \text{K}}{6 * \pi * 0.891 * 10^{-3} \frac{\text{kg}}{\text{m} * \text{s}} * 1.4\ \text{nm}} = 175 \frac{\mu\text{m}^2}{\text{s}}$$

Considering a diffusion time of 20 minutes and a one-dimensional diffusion process ($n = 1$), the typical travel distance for such a molecule species is

$$x = \sqrt{2 * 175 \frac{\mu\text{m}^2}{\text{s}} * 1200\ \text{s}} = 648\ \mu\text{m}\ .$$

16. Penetration behavior of nanoparticles into reconstituted MUC5AC gels

To compare the penetration behavior of nanoparticles into reconstituted mucin gels with the penetration behavior of dextran molecules, the penetration efficiency of cationic and PEGylated particles was investigated. Therefore, commercial amine-terminated polystyrene particles (diameter: 100 nm; label: green fluorescing dye with an excitation wavelength of $\lambda_{480\ \text{nm}}$ and an emission wavelength of $\lambda_{501\ \text{nm}}$) were obtained (Magsphere Inc., Pasadena, CA, USA) at a stock solution concentration of 2.5 % (w/v). For polyethylene glycol (PEG) coating of amine-modified particles, the particles were diluted 1:10 in ultrapure water. A 10-fold excess of α-methoxy-PEG-succinimidyl active ester (Rapp Polymere, Tübingen, Germany) was added to the particle suspension, and the PEGylation reaction was allowed to take place at room temperature overnight. Successful PEGylation was verified by determining the ζ-potential of the modified particles. Size and ζ-potential were measured with dynamic light scattering and laser Doppler anemometry, respectively, using a Zetasizer Nano ZS (Malvern Instruments, Herrenberg, Germany). For those measurements, the particles were diluted 1:100 in 10 mM acetate buffer (pH 4).

Table S1: Particle size, polydispersity index (PDI), and particle surface potential (ζ-potential) of aminated and PEGylated nanoparticles (suspended in 10 mM sodium acetate buffer) as obtained from dynamic light scattering and laser Doppler anemometry at pH 4.0.

Particle type	Particle size [nm]	PDI	ζ at pH 4.0 [mV]
PEGylated	450.1	0.424	-4.0 ± 0.7
Aminated	93.8	0.056	45.7 ± 1.3

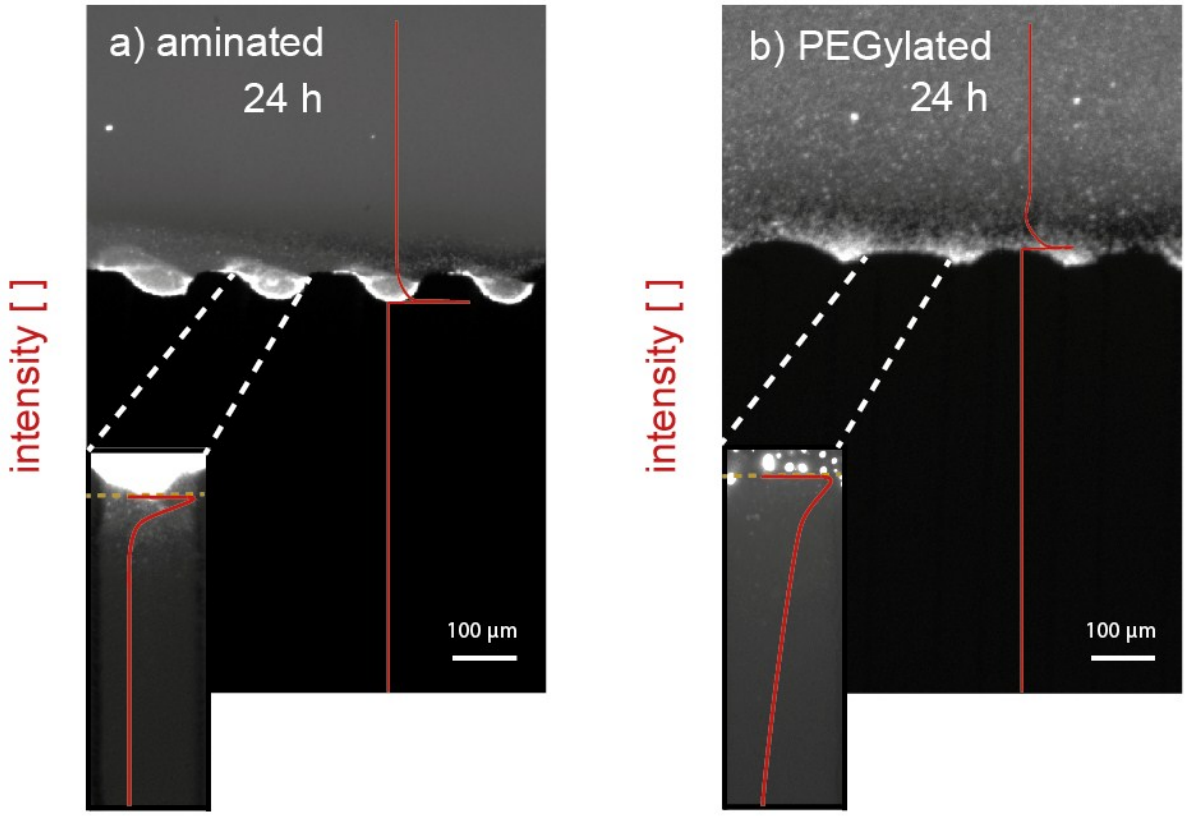

Figure S14: Penetration behavior of nanoparticles into porcine gastric mucin gels reconstituted at a mucin concentrations of 1 % (w/v). The penetration efficiency of amine-terminated (cationic) (a) and PEGylated (neutral) (b) nanoparticles was investigated in the same microfluidics setup used for molecular penetration experiments. Cationic nanoparticles accumulated very strongly at the gel/buffer interface, and only few particles could penetrate the mucin gel (a) as indicated by the sharp decrease in the fluorescence signal. The PEGylated neutral particles formed aggregates and accumulated at the PDMS pillars (b), which prevented an accurate quantitative comparison with the cationic nanoparticles. However, the softly decaying intensity profile obtained for the PEGylated nanoparticles is in marked difference to the profile obtained for the cationic nanoparticles. This indicates that the neutral PEGylated nanoparticles could penetrate the mucin gel at higher numbers and reached larger penetration depths than their cationic counterparts.